The Formation and Stability of Lines Produced by Inkjet Printing

Jonathan Stringer and Brian Derby.*

School of Materials, University of Manchester, Grosvenor Street, Manchester, M1 7HS, UK.

RECEIVED DATE (to be automatically inserted after your manuscript is accepted if required according to the journal that you are submitting your paper to)

CORRESPONDING AUTHOR FOOTNOTE

Jonathan Stringer, Jonathan.Stringer@Manchester.ac.uk, Tel. +44 1613063583

ABSTRACT

In order to produce stable lines with parallel sides through inkjet printing, individual drops are deposited on a surface so that they coalesce; this initial liquid line (or bead) must remain stable until it forms a solid. The stable line width is shown to be bounded by two limits, with the lower bound (minimum line width) determined by the maximum drop spacing for stable coalescence and the upper bound determined by the minimum drop spacing below which a bulging instability occurs. The maximum stable track width is also a function of the velocity at which an inkjet printhead traverses the substrate. These bounds are presented in dimensionless form and shown to agree well with experiment. To enable easier determination of the stability of an arbitrary ink/substrate combination, both the upper and lower bounds are presented in graphical forms to define a region of bead stability in an appropriate parameter space.

Introduction

There has been considerable interest in recent years in the use of inkjet printing as a tool to fabricate engineered objects with applications in a range of fields including, polymers, [1,2] displays, [3] polymer electronics, [4] 3-Dimensional fabrication, [5] and biomaterials and tissue engineering. [6] Unlike the original application of inkjet printing for graphic output, where a pattern of discrete printed drops is required, these new applications often require the coalescence of printed drops to produce linear features, 2-Dimensional patterns or even 3-Dimensional objects. The end product of the printing process for most applications will be a solid deposit, thus for the case of drop coalescence to form a defined shape, stability must be retained from initial coalescence and throughout the subsequent solidification process. Thus the conditions that lead to stable liquid beads on flat substrates must be understood if inkjet printing is to be used as a general fabrication tool.

It has been known for some time that a line or bead of liquid resting on a flat homogeneous surface can be unstable depending on the boundary conditions at the moving contact line. Davis considered the stability of three cases of liquid beads: [7] i) where the contact angle at the line is fixed but the contact line is free to move, ii) where the contact angle is a function of line speed but has a limiting value at zero contact line speed, and iii) where the contact angle is free to change but the contact line is pinned and the two lines defining the liquid bead are parallel. It was shown that for both cases (i) and (ii) a liquid bead undergoes a Rayleigh instability but for case (iii) the bead is stable if the contact angle $\theta < \pi/2$. This prediction was studied by Schiaffino and Sonin who confirmed Davis's predictions using experiments with wax droplets on a cooled substrate such that the contact line was pinned by solidification. [8] They also studied water droplets and found that the liquid bead was always unstable as predicted by Davis's cases (i) and (ii).

In earlier work we considered a lower bound limiting conditions for the width of a stable liquid bead formed through the coalescence of liquid droplets in the case of receding contact line pinning. [9,10] By assuming that liquid beads form through the interaction of adjacent droplets resting on a substrate, a model based on volume conservation was derived that predicted the width of a parallel sided liquid bead as a function of droplet spacing or dot pitch.. The predictions of the model were found to agree well with experiment for a commercial soluble silver ink on a range of substrates. This model assumed that the limiting condition for bead formation was given by a critical amount of droplet overlap.

Duineveld considered another instability that occurs with liquid beads if there is significant hysteresis between the advancing and receding contact angles, θ_a and θ_r respectively. [11] When a liquid contains particles in suspension, or a high concentration of solute, the contact line can be pinned by solid deposition following solvent evaporation resulting in a zero or near zero receding contact angle [12,13] and thus Duineveld's instability analysis may be more appropriate for inkjet printing systems. In this case the instability is present when capillary spreading occurs more rapidly than flow along the direction of printing and results in a characteristic regular spacing of bulges separated by constant section liquid beads. The physical basis for this instability will be considered in more detail as part of this work but this instability defines a maximum droplet overlap for stable liquid bead formation whereas the stability criterion of Stringer [9,10] defines a minimum droplet overlap

Soltman and Subramanian considered the stability of inkjet printed lines in terms of these two instability criteria. [14] They re-derived the lower bound instability criterion in order to present it in a dimensionless form normalized by initial droplet diameter. They also identified the dynamic nature of Duineveld's instability and proposed a qualitative schematic parameter space in which one axis was the spacing of printed droplets on a substrate and the second axis was in temporal units related to the time between adjacent droplet depositions. However, no attempt was made to quantify the model predictions or to test them experimentally.

This work develops the models for the stability of inkjet printed lines presented earlier by ourselves and by Duineveld. The two regimes of line stability provide lower and upper bounds for the width of a stable parallel sided liquid bead. The lower bound is based on the interaction between equilibrium surface tension concepts and contact line pinning, [9,10] the other bound is developed from Duineveld's model that considers a kinetic instability during the deposition and coalescence of drops. [11] These results can be combined and presented in a graphical form that defines a region of stability in appropriate parameter space that can be used with arbitrary ink/substrate combinations.

Criteria for Printed Line Stability

Droplet Equilibrium and Line Stability

Once deposited on a substrate, a liquid droplet will spread to equilibrium defined by the interfacial energy balance of the Young Equation such that:

$$\sigma_{SV} = \sigma_{LS} + \sigma_{LV} \cos\theta_{eqm} \tag{1}$$

where σ_{SV}, σ_{LS} and σ_{LS} are the substrate-vapor, liquid-substrate and liquid vapor surface energies respectively and θ_{eqm} is the equilibrium contact angle. In the case of a finite contact angle, it is possible to model the deposited droplet as a spherical cap if gravitational forces are negligible, i.e. a Bond number ($Bo = \rho g d_0^2 / \sigma_{LV}$) significantly less than 1, where ρ is the liquid density, g is gravitational acceleration and d_0 is the diameter of the drop before it is in contact with the surface. If we assume volume conservation between the deposited drop and the spherical cap, the following expression can be

derived, [15] where β_{eqm} is the diameter of the spherical cap on the substrate, d_{eqm}, normalized to the initial droplet diameter, d_0:

$$\beta_{eqm} = \frac{d_{eqm}}{d_0} = \sqrt[3]{\frac{8}{\tan\frac{\theta_{eqm}}{2}\left(3+\tan^2\frac{\theta_{eqm}}{2}\right)}} \tag{2}$$

With inkjet printing, this liquid cap will eventually transform into a solid either through drying (evaporation) or phase change (solidification). In solidifying systems there is a small change in volume associated with the phase change; in evaporating systems, there could be a significant amount of volume loss before the droplet assumes the equilibrium spherical cap shape, with the amount of volume loss dependent upon the volatility of the droplet. The degree to which this loss of volume affects the final deposit diameter will depend upon whether contact line pinning occurs with the particular evaporating system involved. However, the ubiquitous nature of contact line pinning in all but the cleanest, pure solvent systems would suggest that it is likely to take place in most practical cases of ink jet printing. [12,13]

Two droplets deposited so that they overlap will tend to coalesce. These droplets will coalesce into a single body of liquid if the first deposited droplet does not form a solid before the next one is deposited. A series of droplets deposited linearly on a substrate will therefore form a liquid bead on the substrate. Assuming that the contact line of this liquid bead cannot recede due to contact line pinning, ignoring any end effects and that gravitational forces are negligible (Bo<<1), the bead will have a constant cross section of a circular segment. Based on these assumptions and that of volume conservation between the impinging droplets and the liquid bead, it is possible to construct a simple geometric model of the bead as a function of initial droplet diameter d_0, droplet spacing p, bead width w and θ_{eqm} [9] (figure 1):

$$\frac{\pi d_0^3}{3p} = \frac{w^2}{2}\left(\frac{\theta_{eqm}}{sin^2\,\theta_{eqm}} - \frac{cos\,\theta_{eqm}}{sin\,\theta_{eqm}}\right) \tag{3}$$

By rearranging equation 3 to make w the subject, the following expression for the stable bead width as a function of p, d_0 and β_{eqm} can be obtained: [10]

$$w = \sqrt{\frac{2\pi d_0^3}{3p\left(\frac{\theta_{eqm}}{sin^2\,\theta_{eqm}} - \frac{cos\,\theta_{eqm}}{sin\,\theta_{eqm}}\right)}} \tag{4}$$

The bead width can be normalized with respect to $\beta_{eqm}d_0$, giving the following dimensionless relationship for all stable bead widths:

$$w^* = \frac{w}{\beta_{eqm}d_0} = \sqrt{\frac{2\pi d_0}{3p\beta_{eqm}^2\left(\frac{\theta_{eqm}}{\sin^2\,\theta_{eqm}} - \frac{\cos\,\theta_{eqm}}{\sin\,\theta_{eqm}}\right)}} \tag{5}$$

where w^* is the dimensionless bead width. Assuming that the contact line of an individual droplet is pinned and cannot retract, the minimum width of the bead is equal to $\beta_{eqm}d_0$. By substituting this into equation 5 for w and rearranging, the following equation for the maximum droplet spacing p_{max} is obtained:

$$p_{max} = \frac{2\pi d_0}{3\beta_{eqm}^2\left(\frac{\theta_{eqm}}{sin^2\,\theta_{eqm}} - \frac{cos\,\theta_{eqm}}{sin\,\theta_{eqm}}\right)} \tag{6a}$$

or in dimensionless form using the same normalization as w^*:

$$p^*_{max} f(\theta_{eqm}) = \frac{2\pi}{3} \tag{6b}$$

where

$$f(\theta_{eqm}) = \beta^3_{eqm}\left(\frac{\theta_{eqm}}{\sin^2\theta_{eqm}} - \frac{\cos\theta_{eqm}}{\sin\theta_{eqm}}\right) \tag{6c}$$

Dynamic Line Stability

As discussed earlier, a further bulging instability is observed at smaller droplet separation, which consists of a series of bulges connected by ridges of width $\beta_{eqm}d_0$. Duineveld proposed that the transition to this morphology was explained by competing flow rates within the bead. There is a flow, Q, along the bead driven by a pressure difference from any variation in bead width. There is another spreading flow, Q_A, due to capillarity. [11] If $Q >> Q_A$, any newly deposited liquid will preferentially flow along the bead to the area of low pressure, rather than causing the bead to spread. Here we present Duineveld's model and develop it further to present an explicit analytical expression for the onset of the bulging instability.

Duineveld's analysis assumes that Q_A is the mean flow rate generated by droplet deposition, which is significantly less than the axial flow due to pressure differences within the bead:

$$Q_A << Q \tag{7a}$$

or

$$K_1 Q_A < Q \tag{7b}$$

where K_1 is a constant > 1, which we have introduced for convenience in later manipulation. Q_A can be defined as the rate of arrival of drops from the printer

$$Q_A = V_D f = \frac{V_D U_T}{p} = \frac{\pi d_0^3 U_T}{6p} \tag{8}$$

where V_D is the volume of a droplet, f is the frequency of droplet generation and U_T is the speed at which the substrate moves relative to the printhead. It is also assumed that the axial flow within the bead is fully developed and dominated by viscous forces, with a zero shear stress condition on the free (bead/vapor) surface. From this Duineveld obtained the following expression for Q: [11]

$$Q = \frac{4S\Delta P_R A_R^2}{\eta l_r} \tag{9}$$

where ΔP_R is the pressure difference between the ridge and the bulge, A_R is the cross sectional area of the ridge, η is the dynamic viscosity of the liquid, l_r is the length of ridge between newly deposited droplets and a bulge, and S is a shape factor with:

$$S = \frac{\theta_c - \sin\theta_c \cos\theta_c}{8(\sin\theta_c + \theta_c)^2} \tag{10}$$

where θ_c is the contact angle of the ridge with the substrate. If a bulge forms, $\theta_c < \theta_{eqm}$ to eliminate the driving force for capillary spreading within the ridge, it is therefore assumed in this work that the critical criterion for which the axial flow will dominate and bulges appear is $\theta_c = \theta_{eqm}$.

The low pressure region, at which the bulge will form, occurs because of a difference in width between a newly deposited droplet and some point further down the bead. Duineveld considered the evolution of this pressure difference in some detail but for his calculations of fluid flow within a liquid bead he used the approximate value $\Delta P_R = 2\sigma_{LV} \sin\theta_{eqm} / \left(\beta_{eqm} d_0\right)$. We use the following argument to determine the pressure difference. The most obvious difference in width along a bead is caused by the bead spreading to a stable width, *w*. The pressure difference between a ridge of width $\beta_{eqm}d_0$ and a bead of width *w* is given below:

$$\Delta P_R = P_w - P_{\beta_{eqm}d_0} = \frac{2\sigma_{LV} \sin\theta_{eqm}\left(w - \beta_{eqm} d_0\right)}{w\beta_{eqm} d_0} = \frac{2\sigma_{LV} \sin\theta_{eqm}}{\beta_{eqm} d_0} \frac{\left(w^* - 1\right)}{w^*} \tag{11}$$

The length of ridge, l_r, over which equation 11 will be valid depends on the rate of capillary spreading of the bead. Duineveld estimated the spreading time of the coalesced droplets to a bead of width *w* to be of the order of 100 ms. [11] This estimate is contingent on the properties of the fluid, in particular the dynamic viscosity and surface tension, and the rate of phase change of the fluid. A more viscous fluid will spread at a slower rate than a less viscous fluid, [16] and this can be exacerbated by any evaporation that reduces solvent content. The value of l_r is also found to decrease with increasing U_T. While highly simplified, considering the interplay of various factors outlined above, the value of l_r in this work is assumed to be proportional to the drop spacing, *p*, leading to the following equation:

$$l_r = K_2 p \tag{12}$$

The cross-sectional area of the ridge, A_R, is given by conservation of mass within the bead with:

$$A_R = \frac{\pi d_0^3}{6p} \tag{13}$$

By substituting equations 8, 9, 10, 11, 12, 13 and into inequality 7, the following inequality is derived:

$$\frac{\eta U_T}{\sigma_{LV}} > \frac{4\pi S \sin\theta_{eqm}}{3\beta_{eqm} K_1 K_2} \frac{d_0^2}{p^2} \left(\frac{w^* - 1}{w^*} \right) \tag{14}$$

This can be rewritten in terms of dimensionless drop spacing, p^*, by substituting for w^* (equations 5 and 6) to give

$$\frac{\eta U_T}{\sigma_{LV}} > \frac{4\pi S \sin\theta_{eqm}}{3\beta_{eqm\,eqm}^3 K_1 K_2} \frac{1}{\left(p^*\right)^2} \left(\frac{\sqrt{\frac{2\pi}{3p^* f(\theta)}} - 1}{\sqrt{\frac{2\pi}{3p^* f(\theta)}}} \right) \tag{15}$$

In inequality 15 the terms S, β_{eqm} and $f(\theta_{eqm})$ are all functions of θ_{eqm} and both K_1 and K_2 are constants, hence we can express inequality 14 in terms of a simple function of p^* and θ_{eqm}.

$$U_T^* > g\left(p^*, \theta_{eqm}\right) \tag{16a}$$

where

$$U_T^* = \frac{\eta U_T}{\sigma_{LV}} \tag{16b}$$

and $$g\left(p^*,\theta_{eqm}\right)=\frac{4\pi S\sin\theta_{eqm}}{3\beta_{eqm}^3K_1K_2}\frac{1}{\left(p^*\right)^2}\left(\frac{\sqrt{\frac{2\pi}{3p^*f\left(\theta_{eqm}\right)}}-1}{\sqrt{\frac{2\pi}{3p^*f\left(\theta_{eqm}\right)}}}\right) \quad (16c)$$

Thus the inequality can be considered as representing the relationship between a dimensionless velocity for the traverse of an inkjet printer (U_T*) and a dimensionless drop spacing raised to the power of -2 (modified by a function of the equilibrium contact angle). Unstable lines are formed when the drops are placed too close together but this threshold is reduced as the traverse velocity increases. We note that the dimensionless velocity, U_T*, has the same dimensional form as the Capillary number.

This representation of Duineveld's model for the onset of the bulging instability, although somewhat simplified, allows it to be stated in the form of an analytical expression that can be used to determine the critical droplet spacing for the onset of the instability at a given line speed, as a function of the equilibrium contact angle.

Experimental

The inks used in this study were a commercial silver nanoparticle ink (Inkjet Silver Conductor AG-IJ-G-100-S1, CABOT-PED, Albuquerque, NM, USA; herein referred to as nanoparticle ink) and an organometallic salt dissolved in xylene synthesized in-house (herein referred to as organometallic ink). Preparation details for the synthesis of the organometallic solution have been published previously. [17] The substrates used in this study were glass (microscope slides, BDH, Poole, Dorset, UK), polyimide film (Kapton™, DuPont, Wilmington, DE, USA) and silicone rubber (Goodfellow Cambridge Ltd., Huntingdon, UK). The equilibrium contact angle, θ_{eqm}, of each ink/substrate combination was measured using a CCD camera and image analysis software (FTA 200, Camtel, Royston, UK). Both

inks used have previously been characterized with regards to surface tension and viscosity, either in previous publications or on data sheets supplied with the ink. This data is summarized in Table 1.

Printing of samples was carried out using a JetLab printing platform (MicroFab Inc., Plano, TX, USA) that consists of a piezoelectric squeeze mode printhead situated above a programmable *x-y* platform. The printheads used in this study had a nozzle diameter of 50 μm (MJ-SF-01-50, MicroFab). It is possible to alter printed drop velocity by controlling the shape and timing of the electrical pulse used to actuate the piezoelectric printhead. Table 2 shows the conditions used to actuate the printer for the materials used and that for the organometallic ink we used two different drop velocities. Droplet diameter measurements were conducted by ejecting a known number of droplets into a vial containing an appropriate solvent. The mass change of this vial was compared with an identical reference vial filled with the same solvent and a mass balance used to calculated the diameter of an individual droplet, assuming a spherical droplet and known density values. All substrates were cleaned with acetone before deposition of droplets.

Variation of p and U_T, leads to a corresponding variation of the droplet deposition frequency, f. As f is increased, it is possible that there may be acoustic interference (constructive or destructive) within the printhead that influence the size and velocity of ejected droplets. [18] For this reason, values of d_0 were measured for all frequencies used.

Results and Discussion

Stable bead formation from overlapping droplets

In order to explore the transition from isolated drops to a stable bead, we printed a series of deposits with overlapping droplets of both the organometallic and nanoparticle ink on glass, polyimide and silicone substrates, using printing condition 1 (Table 2), with droplet spacing of the beads varying between values approximately 15 μm below p_{max} (equation 6) and $\beta_{eqm}d_0$ (equation 2).

Figures 2 and 3 show typical morphologies either side of p_{max} for the organometallic ink on glass and silicone substrates. In both cases the deposit morphology for samples just below $p = p_{max}$ is that of a stable track with parallel contact lines. Above p_{max} the morphology of the samples on high contact angle substrates (figure 3) is in good agreement, with a periodic curvature to the contact line, as there is insufficient fluid to form a stable bead. A similar behavior is seen with the nanoparticle ink on all substrates. However, on the low contact angle substrates (figure 2) equation 6 does not give such an accurate prediction for the transition between the two morphologies, with the change in morphology found to occur at higher values of p. This is believed to be related to the behavior shown in figure 4 where it can be seen that adjacent printed droplets have spread to an elliptical footprint and approached each other; with the result in one instance that droplet coalescence has occurred even though $p > \beta_{eqm}d_0$. This phenomenon is believed to be related to local changes in surface energy related to vapor transport from the drops but further work is required to confirm this. Similar observations of excess droplet spreading in the printing direction and the influence it has on bead morphology have been made for a study of the inkjet printing of an aqueous solution of poly(3,4-ethylene-dioxythiopene)poly(styrenesulfonate), PEDOT/PSS. [14] While this shows that it is possible to form stable tracks from droplets spaced with $p > \beta_{eqm}d_0$, there is no benefit gained in terms of smaller features because contact line pinning limits the minimum track width to $\beta_{eqm}d_0$.

To study the relation between droplet spacing and stable bead width, and to validate equation 5, we printed a series of beads of organometallic ink at constant frequency (750 Hz), using printing condition 1 (Table 2), onto glass, polyimide and silicone substrates. In all cases the same qualitative behavior was observed, with the deposited bead width decreasing as p increases. The beads formed on polyimide showed significantly greater width, w, for a given drop spacing p, than the deposits formed on glass; those formed on silicone did not show spreading to the same degree as with the other substrates. This is to be expected as the contact angle of the organometallic ink on glass is intermediate to that on polyimide and silicone (Table 3). The range of drop spacing in which stable beads were produced on silicone was relatively small, with a bulging instability observed at low values of p and break-up of the bead into individual droplets at high p. This small range of stable p occurs because high θ_{eqm} substrates will produce beads that have a low value of p_{max} (equation 6) and are also more likely to possess a bulging instability if all other variables are kept constant. [11] The measured values of w on the silicone substrate did not show such good agreement with equation 5 as the other substrates, with w tending towards $\beta_{eqm}d_0$ in all cases. A possible cause of this could be inaccuracies in either measurement of any the involved variables (w, θ_{eqm}, d_0) being amplified at the smaller size of deposit. We carried out an identical series of experiments using the silver nanoparticle ink with printing condition 3 (Table 2). There is again a strong relationship between deposit width, w, and θ_{eqm}. We found that the measured values of w compare well with those predicted by equation 4, and this was found to hold for all deposits formed from stable beads of nanoparticle ink.

To allow a comparison with prediction for all inks and substrates, the bead width and drop spacing have been converted to the dimensionless terms w^* and $p^*f(\theta)$ and compared with equations 5 and 6 in figure 5. There is good agreement between equation 5 and the experimental results before the threshold given by equation 6 for all combinations of ink and substrate. Above the threshold given by equation 6, the value of w^* becomes constant at a value of 1; This corresponds to $w = \beta_{eqm}d_0$, showing that the

minimum width achievable for a bead formed by ink jet printing is the diameter of a single droplet on a substrate; this is limited by contact line pinning, as discussed previously. The value of p_{max} occurs at a lower value of p as θ_{eqm} is increased, meaning that there is a smaller range of p that is usable to produce stable beads.

Unstable bead formation and bulging

A series of beads of the nanoparticle ink were printed onto three different substrates: glass, polyimide and silicone using condition 3 (Table 2). The bead morphologies observed with the nanoparticle ink are in good qualitative agreement with those expected for a bulging instability (figure 6). The bulging instability was found to be more prevalent on high contact angle substrates, at low p and at low U_T. These data are therefore suitable to be used to identify the undefined constants, K_1 and K_2, in inequalities 14 and 15. The product of the undefined constants can be determined by the best fit of the instability criterion to the data, resulting in $K_1K_2 = 4$. This value is physically consistent with the definitions of both K_1 and K_2. In order to test the validity of the model's predictions, inequality 15, the dimensionless form of the instability criterion, is plotted in figure 7. This divides the parameter space into two regions with stable beads formed at large drop spacing and traverse velocity.

Superimposed upon the stability criterion in figure 7, we have plotted experimental data from our experiments and from sources in the literature. [11,19] Our data for lines printed on polyimide and silicone substrates show two sets of unstable conditions falsely identified as stable. In all cases where the criterion inaccurately predicts the outcome for a given set of deposition conditions on high contact angle substrates, the conditions are very close to the threshold defined by the inequality 14. It is therefore possible that these erroneous results arose from the simplified assumptions made when deriving the inequality. One feature of note is that the criterion erroneously predicts unstable results on the low

contact angle substrate (glass) and stable results on higher contact angle substrates (polyimide and silicone). This could suggest that the modeling of the capillary spreading flow is too simplistic because it assumes instantaneous spreading to $\beta_{eqm}d_0$ and that the spreading from $\beta_{eqm}d_0$ to w has no driving force associated with it that can compete with the pressure-driven axial flow. This discrepancy could also be due to the assumption for the ridge length, l_r, given in equation 12 for the reasons discussed previously.

The model assumes a two stage process of bead formation, whereby any axial flow takes place before the bead spreads due to capillarity, this model would only be valid if the driving force for wetting of the substrate is relatively low or acts over timescales far in excess of any axial flow. On low contact angle substrates the driving force for capillary flow due to the surface energy imbalance will be substantial as more liquid is added, and this two stage assumption may no longer be valid. This would result in capillary-driven spreading dominating where pressure-driven flow would be expected to dominate, resulting in a stable bead where the model would predict differently. This is therefore a possible explanation for our outlying results for glass and Duineveld's results for PEDOT/PSS solutions on a plasma-treated resist substrate that showed a zero receding contact angle.

The morphologies observed for the organometallic ink, while in some ways showing qualitative agreement with the experimental results and predictions of Duineveld, [11] show little quantitative agreement. The bead morphology observed on the low contact angle substrates of glass (figure 8) and polyimide at low drop spacing, p, shows bulges connected by ridges where the ridges have a width significantly greater than $\beta_{eqm}d_0$, and the appearance of bulges seems to be independent of traverse velocity, U_T. Printed beads on a high contact angle substrate (silicone, figure 9) show greater similarity with Duineveld's results, with ridge widths approximating to $\beta_{eqm}d_0$ and bulges first observed at larger p as U_T is increased. It should, however, be noted that the range of stable bead widths possible on silicone are much smaller according to equation 5 and at all but the smallest values of p are very close to $\beta_{eqm}d_0$.

A possible explanation for this discrepancy is that there is no allowance for evaporation in Duineveld's model. [11] Assuming that the evaporation time of a droplet is limited by diffusion of the solvent away from the droplet, a simple order of magnitude estimate for the evaporation time, t_e, necessary for the contact line to be permanently pinned can be obtained by:

$$t_e \approx \frac{K_3 \rho d_0^2}{D_V C_V} \tag{17}$$

Where D_V is the vapor diffusion coefficient, C_V is the saturated vapor concentration and K_3 is a constant representing the fraction of solvent evaporation necessary for precipitation to take place (in this case, $K_3 = 0.02$). In this work the solvent used was xylene which has the following values for saturated vapor concentration and diffusion coefficient: $C_v = 3.6 \times 10^{-2}$ kgm^{-3}, $D_v = 7.5 \times 10^{-6}$ m^{2}s^{-1} (manufacturer's data, Sigma Aldrich Ltd, Dorset, UK). Using equation 17, an evaporation timescale, t_e, of approximately 50 ms is thus obtained. This is of a similar order of magnitude to the time necessary for a deposited liquid bead to spread, [16] and it is thus possible that evaporation will have an influence on the dynamics of bulge formation. The poor agreement with Duineveld's model for high vapor pressure inks is discussed in more detail elsewhere.[20] It should also be noted that, due to the relatively long time between droplet depositions, that such mechanisms may explain the outlying results in figure 7 from Duineveld's data.

Graphical Representation of Printed Line Stability

From the results we have presented, we have demonstrated that the stability of liquid beads, and hence inkjet printed continuous lines, is controlled by two limiting conditions related to drop spacing

and printer traverse velocity. From the grouping of the variables of inequality 16, it is possible to construct a stability map, with axes of $g(p^*, \theta_{eqm})$ and U_T^*, to enable graphical inspection of a given set of printing parameters to see whether a stable liquid bead will form. The inequality will be represented by a diagonal line of this graph (as in figure 7) with the region for stable bead formation lying above and to the left. The x-axis of the map represents a dimensionless function of the drop spacing and thus it will be possible to use the threshold defined in equation 6 to identify a vertical line that represents p^*_{max}, the dimensionless maximum drop spacing. We also note that the y-axis represents a dimensionless traverse velocity of the printing system. Although there is no physical limit to this velocity implicit in our analysis, any given printing system will have a maximum traverse velocity that is defined by its design and/or construction. Thus we would expect the stability map to be a triangular region in this version of the parameter space (figure 10) with a diagonal line indicating the bulge instability, a vertical line the maximum drop spacing for line formation and a horizontal line indicating the mechanical limitations of the printing system.

In order to determine values for these thresholds and to maintain self-consistency with the representation of the bulging instability, we must make some alterations to our previous analysis of p_{max}. The assumption of $w = \beta_{eqm} d_0$ used to determine p_{max} (equation 6) is not consistent with equation 11, because, in its present form, it implies that there is no pressure difference within the bead. While this would simplify the creation of a stability map, it does not give any indication as to the relative sensitivity of the deposited bead to the development of any instability with varying θ_{eqm}. For this reason we arbitrarily define $w = 1.1\beta_{eqm} d_0$, which both allows for variation of w with θ_{eqm} and gives a small pressure difference within the bead to drive axial flow, thus making the right hand side of inequality 14 greater than zero. The choice of this value also makes the stability map more robust to any positioning errors that may occur. By substituting the appropriate value of p into equation 16e, an expression for a threshold representative of p_{max} can be derived:

$$g\left(p^*_{\max},\theta_{eqm}\right)=\frac{0.127\beta^3_{eqm}S\sin\theta_{eqm}}{K_1K_2}\left(\frac{\theta_{eqm}}{\sin^2\theta_{eqm}}-\frac{\cos\theta_{eqm}}{\sin\theta_{eqm}}\right)^2 \tag{18}$$

From the definitions of β_{eqm} (equation 2) and S (equation 10), this threshold is dependent only upon the equilibrium contact angle, θ_{eqm}, and the value of K_1K_2.

The traverse velocity limit corresponds to the maximum attainable value of the left hand side of inequality 16a, which is given by:

$$U^*_{T\max}=\frac{\eta U_{T\max}}{\sigma_{LV}} \tag{19}$$

where U_{Tmax} is the maximum speed at which the substrate can move relative to the printhead (defined by the relevant parameters of the printing equipment under study). If we use typical values for the viscosity of an ink suitable for inkjet printing, η < 10 mPas and σ_{LV} < 50 mJm^{-2}, we would expect $U^*_{T\max}$ < 1 for most practical printing systems.

By plotting inequality 16a and equations 18 and 19 on a common set of axes, a triangular region is defined within which a stable liquid bead is be produced (figure 10). Unfortunately, because of the assumptions used in the definitions of the two stability bounds, it is impossible to produce a plot that is both dimensionless and independent of the contact angle, θ_{eqm}. The position of the vertical line that indicates the maximum drop spacing on the substrate is an additional function of θ_{eqm} as can be seen in figure 10. However the position of the bulging instability is invariant with contact angle using this system of axes. From this figure we can see that the triangular region of stability is a function of θ_{eqm}, with low equilibrium contact angle drop/substrate combinations showing the largest region of stability.

Although this plot (figure 10) is useful in identifying the conditions for stable printing, the rather artificial formulation of $g(p^*_{max}, \theta_{eqm})$ makes it difficult to visualize how the printing parameters and contact angle each influence line stability. In figure 11 we have replaced the x- axis with drop spacing normalized by printed drop diameter (p/d_0) and redrawn the stability map with the new axis set. Using this representation, the loci representing both of the stability criteria appear as functions of the contact angle. However, it is easier to appreciate the inter-relation between drop spacing and printhead traverse velocity that defines the onset of the bulging instability. It can now be clearly seen that the region of stability is reduced as the contact angle of the drop on the substrate increases and that increasing the velocity of traverse allows stable lines with smaller drop spacing and hence thicker printed lines.

Conclusions

We have shown that when liquid drops show contact line pinning, it is possible to form stable lines or liquid beads, with constant width and parallel, straight edges, through the coalescence of trains of overlapping drops. The conditions for stable line formation are limited by upper and lower bounds for drop width, which can be predicted through simple mechanism models for the bounding instabilities. These bounds can be also considered in terms of critical drop spacing (dot pitch) with the lower bound for width determined by a maximum drop spacing and the upper bound by a minimum drop spacing. The upper bound is also a function of the rate at which the drops arrive at the surface, with a more rapid delivery leading to a larger stable upper bounding bead width. It is possible to describe these two limiting bounds using a common dimensionless formulation and produce a graphical prediction of the conditions for track stability. These predictions have been compared with experimental results and show good agreement with a range of ink and substrate combinations in this study and in the literature.

However, with an ink based on a relatively high vapor pressure solvent, the agreement was less good. We found that in this case the maximum drop spacing for overlap and the onset of coalescence is greater than predicted from the shape of isolated drops of fluid spread on a smooth surface. As separated adjacent liquid drops are printed with smaller separations, it is noticeable that the droplet spreading is no longer circular but instead forms an elliptical shape with the long axis of the ellipse along the line of droplet separation. This behavior is more pronounced with higher vapor pressure solvents and with lower contact angles. We hypothesize that this behavior is driven by evaporation from the drops prewetting the region between adjacent droplets and influencing contact line tension. However, this phenomenon needs further investigation. In addition, this high vapor pressure ink did not show the strong morphological transition at small drop spacings and low traverse velocities to the bulging instability first investigated by Duineveld.[11] This divergence in behavior from many reports in the literature[11,14,19] may be because the time constant for evaporation is similar to that for droplet spreading and thus may invalidate some of the assumptions in Duineveld's model for the onset of the instability.

ACKNOWLEDGMENTS This work was partially supported by the Office of Naval Research through project N00014-03-1-0930 and also partly by the EPSRC though project GR/T11920/01.

References

(1) Calvert P. *Chem. Mater*. **2001**, *13*, 3229-3305.

(2) de Gans,B-J.; Duineveld,P.C.; Schubert U.S. *Adv. Mater.* **2004**, *16*, 203-213.

(3) Shimoda, T.; Morii, K.; Seki, S.; Kiguchi, H. *MRS Bull.* **2003**, *11*, 821-828.

(4) Burns, S.E.; Cain, P.; Mills, J.; Wang, J.; Sirringhaus H. *MRS Bull.* **2003**, *11*, 829-835.

(5) Derby, B.; Reis N. *MRS Bull*. **2003**, *11*, 815-820.

(6) Derby, B. *J. Mater. Chem.* **2008**, *18*, 5717 – 5721.

(7) Davis, S. H. *J. Fluid Mech*. **1980**, *98*, 225-242.

(8) Schiaffino, S.; Sonin, A.A. *J. Fluid Mech*. **1997**, *343*, 95-110.

(9) Smith, P.; Dearden, A.; Stringer, J.; Shin, D-Y.; Reis N.; Derby, B. *J. Mater. Sci.* **2006**, *41*, 4153-4158.

(10) Stringer, J.E.; Derby, B. *J. Europ. Ceram. Soc.* **2009**, *29*, 913-918..

(11) Duineveld, P. C. *J. Fluid Mech.* **2003**, *477*:175-200.

(12) Deegan, R.D.; Bakajin, O.; Dupont, T.F.; Huber, G.; Nagel, S.R.; Witten, T.A. *Nature* **1997**, *389*, 827-829.

(13) Deegan, R.D.; Bakajin, O.; Dupont, T.F.; Huber, G.; Nagel, S.R.; Witten, T.A. *Phys. Rev. E,* **2000**, 62, 756-765.

(14) Soltman, D.; Subramanian, V. *Langmuir* **2008**, *24*, 2224-2231.

(15) van Dam, D. B.; Le Clerc, C. *Phys. Fluids*, **2004**, *16*, 3403-3414.

(16) Tanner, L.H. *J. Phys. D: Appl. Phys.*, **1979**, *12*, 1473-1484.

(17) Dearden, A.L.; Smith, P.J.; Shin, D.Y.; Reis, N.; Derby B.; O'Brien, P.; *Macromol. Rap. Comm*. **2005**, *26*, 315-318.

(18) Reis, N.; Ainsley, C.; Derby, B. *J. Appl. Phys* **2005**,. *97*, 094903.

(19) van den Berg, A.M.J.; de Laat A.W.M.; Smith, P.J.; Perelaer, J.; Schubert, U.S. *J. Mater. Chem*. **2007**, *17*, 677-683.

(20) Stringer, J.; Derby, B. *J. Europ. Ceram. Soc.* **2009**, *29*, 913-918.

FIGURE CAPTIONS

Figure 1. At low values of Bond number a series of coalescing isolated drops will form a liquid bead of circular profile.

Figure 2. Printed track morphologies after drying of the organometallic ink on a glass substrate with a range of drop centre spacings around p_{max} = 83.4 μm: a) p = 80 μm b) p = 90 μm and c) p = 120 μm..

Figure 3. Printed track morphologies after drying of the organometallic ink on a silicone substrate with a range of drop centre spacings around p_{max} = 55.3 μm: a) p = 55 μm b) p = 60 μm and c) p = 85 μm..

Figure 4. Inkjet printed droplets of the organometallic ink on glass showing an interaction between neighboring droplets with drop spacings a) p = 300 μm, b) p = 195 μm, c) p = 180 μm, d) p = 165 μm . Solid outline shows position of the contact line with an identical volume isolated drop. In image (d) drop coalescence has occurred even though isolated drops would not touch at that spacing. $\beta_{eqm}d_0$ = 155 μm in all cases.

Figure 5. A plot of normalized bead width, w^*, against normalized droplet spacing, $p^*f(\theta_{eqm})$, for both nanoparticle (filled symbols) and organometallic inks (open symbols) on all substrates. Lines correspond to equations 5 and 6.

Figure 6. Printed track morphologies after drying of the nanoparticle ink on a polyimide substrate with a range of drop centre spacings and printhead traverse velocities:. a) p = 10 μm, U_T = 10 mms^{-1} b) p = 10 μm, U_T = 100 mms^{-1} c) p = 20 μm, U_T = 10 mms^{-1} d) p = 20 μm, U_T = 100 mms^{-1}.

Figure 7: Stability map showing the condition for the onset of the bulging instability as defined by equations 15 and 16, with data for the nanoparticle ink experiments superimposed, together with data obtained from the literature. In all cases, open symbols indicate an unstable morphology and filled marks indicate a stable morphology:

Figure 8. Printed track morphologies after drying of the organometallic ink on a glass substrate with a range of drop centre spacings and printhead traverse velocities:. a) p = 10 μm, U_T = 10 mms^{-1} b) p = 10 μm, U_T = 100 mms^{-1} c) p = 20 μm, U_T = 10 mms^{-1} d) p = 20 μm, U_T = 100 mms$^{-1.}$

Figure 9. Printed track morphologies after drying of the organometallic ink on a silicone substrate with a range of drop centre spacings and printhead traverse velocities:. a) p = 10 μm, U_T = 10 mms^{-1} b) p = 10 μm, U_T = 100 mms^{-1} c) p = 20 μm, U_T = 10 mms^{-1} d) p = 20 μm, U_T = 100 mms^{-1}.

Figure 10 Map of parameter space defined by a dimensionless velocity and a function of p^* and θ, showing the region of printed line stability. The solid diagonal line indicates the onset of the bulging instability. The horizontal dashed line indicates the maximum traverse speed for a particular printing system. The maximum drop spacing limit (vertical dotted line) is shown for a range of equilibrium contact angles.

Figure 11. Alternative representation of the regions within which inkjet printed liquid lines or beads are stable using dimensionless axes of velocity and drop spacing for a range of contact angles. The curved lines show the onset of the bulging instability and the vertical lines show the limit of maximum droplet spacing. The region of stability clearly gets smaller and the range of stable droplet spacing reduces as the contact angle increases.

Table 1. Fluid physical properties of the inks used in this study.

Ink	Viscosity, η mPa.s	Surface Tension, σ_{LV} $mJ.m^{-2}$
Nanoparticle	14.4	31
Organometallic	4.14	28

Table 2. Piezoelectric actuation pulse for the inkjet printheads and the resulting drop diameter and drop ejection velocity.

Ink	Condition	Voltage V	Rise time µs	Dwell time µs	Fall time µs	d_0 µm	Velocity ms^{-1}
Organometallic	1	50	5	50	5	65	2.3
Organometallic	2	90	5	60	5	72	4.8
Nanoparticle	3	60	10	60	10	56	2.8

Table 3. Contact angle of the inks on the substrates used in this study.

Ink	Substrate	θ /°
Nanoparticle	Glass	7.8 ± 2.2
Nanoparticle	Polyimide	45.2 ± 0.8
Nanoparticle	Silicone	63.4 ± 1.1
Organometallic	Glass	22.0 ± 1.4
Organometallic	Polyimide	10.8 ± 2.4
Organometallic	Silicone	75.0 ± 1.3

Figures

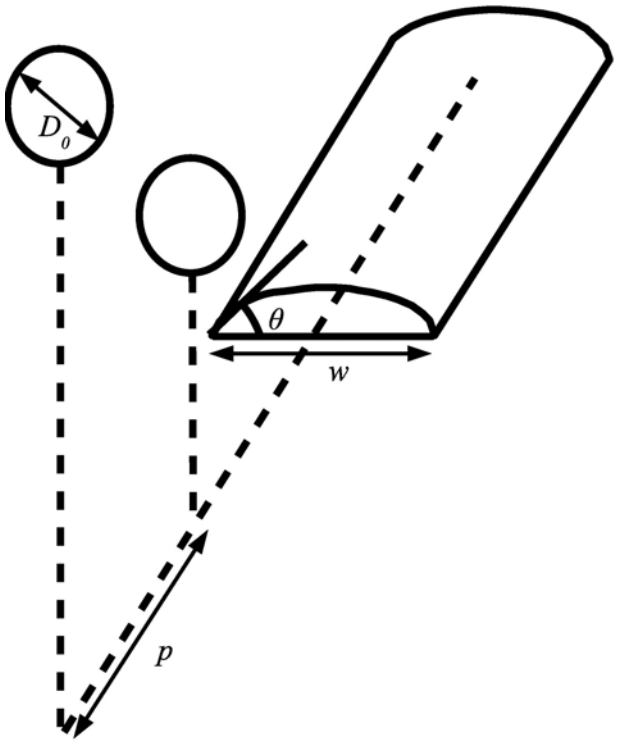

Figure 1. At low values of Bond number a series of coalescing isolated drops will form a liquid bead of circular profile.

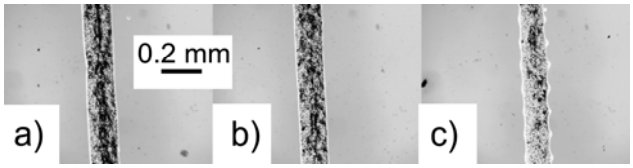

Figure 2. Printed track morphologies after drying of the organometallic ink on a glass substrate with a range of drop centre spacings around p_{max} = 83.4 μm: a) p = 80 μm b) p = 90 μm and c) p = 120 μm.

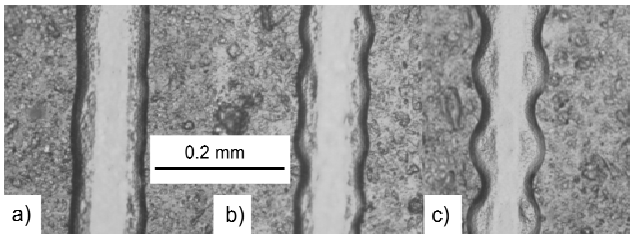

Figure 3. Printed track morphologies after drying of the organometallic ink on a silicone substrate with a range of drop centre spacings around p_{max} = 55.3 μm: a) p = 55 μm b) p = 60 μm and c) p = 85 μm.

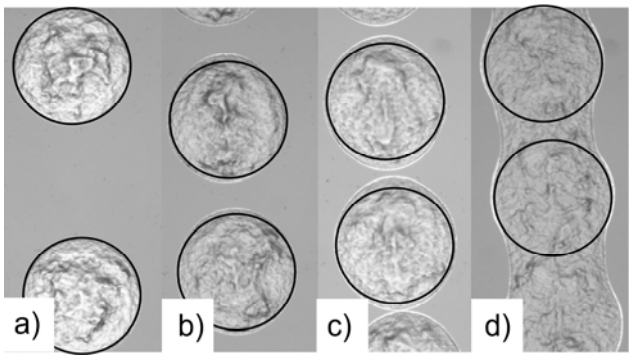

Figure 4. Inkjet printed droplets of the organometallic ink on glass showing an interaction between neighboring droplets with drop spacings a) p = 300 μm, b) p = 195 μm, c) p = 180 μm, d) p = 165 μm. Solid outline shows position of the contact line with an identical volume isolated drop. In image (d) drop coalescence has occurred even though isolated drops would not touch at that spacing. $\beta_{eqm}d_0$ = 155 μm in all cases.

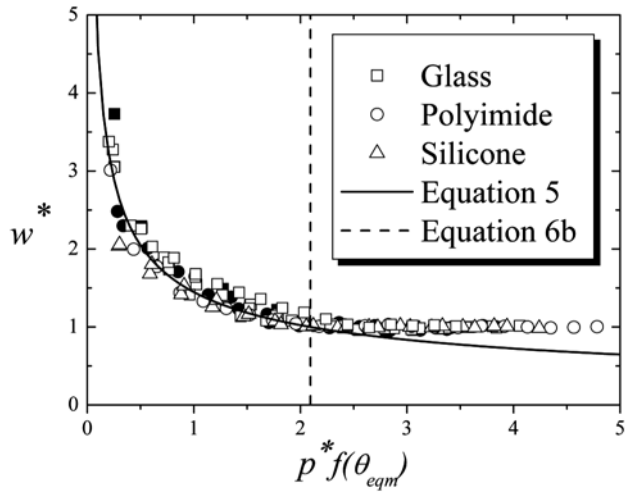

Figure 5. A plot of normalized bead width, w^*, against normalized droplet spacing, $p^*f(\theta_{eqm})$, for both nanoparticle (filled symbols) and organometallic inks (open symbols) on all substrates. Lines correspond to equations 5 and 6.

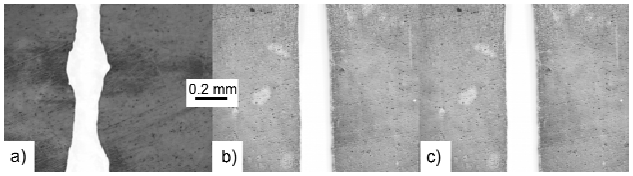

Figure 6. Printed track morphologies after drying of the nanoparticle ink on a polyimide substrate with a range of drop centre spacings and printhead traverse velocities:. a) p = 10 μm, U_T = 10 mms^{-1} b) p = 10 μm, U_T = 100 mms^{-1} c) p = 20 μm, U_T = 10 mms^{-1} d) p = 20 μm, U_T = 100 mms^{-1}

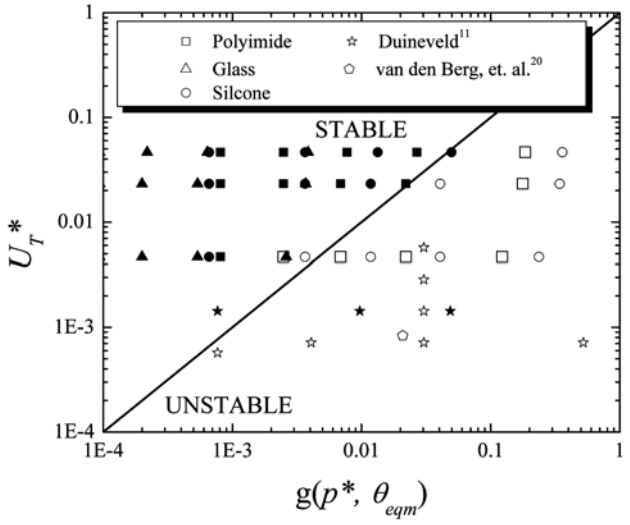

Figure 7: Stability map showing the condition for the onset of the bulging instability as defined by equations 15 and 16, with data for the nanoparticle ink experiments superimposed, together with data obtained from the literature. In all cases, open symbols indicate an unstable morphology and filled marks indicate a stable morphology:

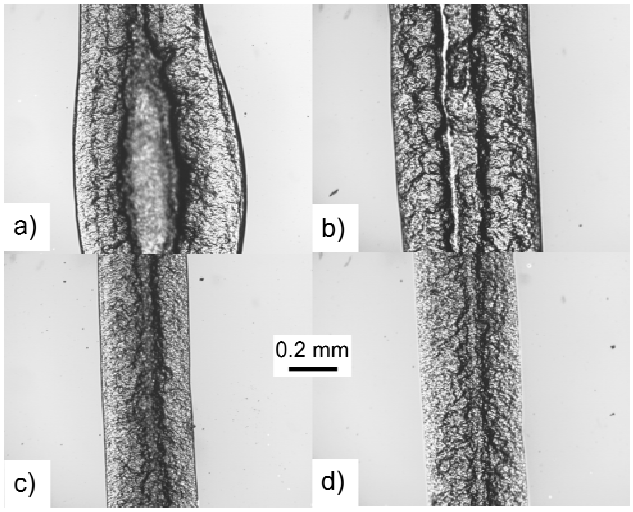

Figure 8. Printed track morphologies after drying of the organometallic ink on a glass substrate with a range of drop centre spacings and printhead traverse velocities:. a) p = 10 μm, U_T = 10 mms^{-1} b) p = 10 μm, U_T = 100 mms^{-1} c) p = 20 μm, U_T = 10 mms^{-1} d) p = 20 μm, U_T = 100 mms^{-1}

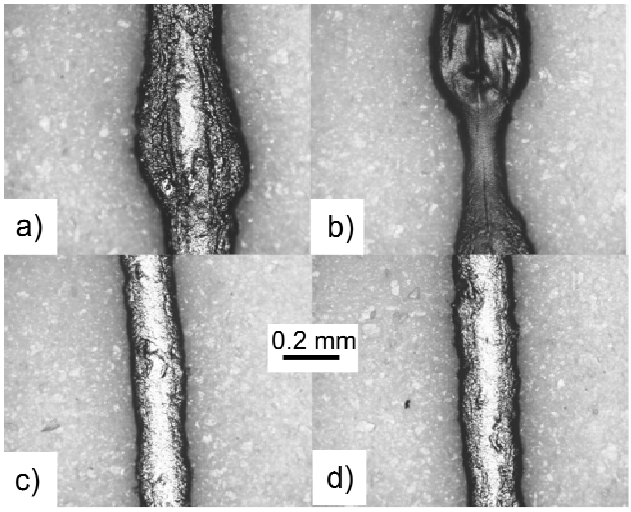

Figure 9. Printed track morphologies after drying of the organometallic ink on a silicone substrate with a range of drop centre spacings and printhead traverse velocities: a) p = 10 μm, U_T = 10 mms^{-1} b) p = 10 μm, U_T = 100 mms^{-1} c) p = 20 μm, U_T = 10 mms^{-1} d) p = 20 μm, U_T = 100 mms^{-1}

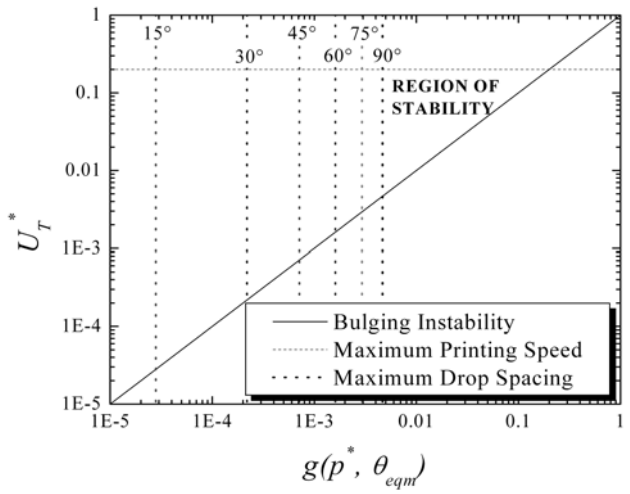

Figure 10 Map of parameter space defined by a dimensionless velocity, U_T^*, and a function, $g(p^*, \theta_{eqm})$, of dimensionless drop spacing, p^*, and equilibrium contact angle, θ_{eqm}, showing the region of printed line stability. The solid diagonal line indicates the onset of the bulging instability. The horizontal dashed line indicates the maximum traverse speed for a particular printing system. The maximum drop spacing limit (vertical dotted line) is shown for a range of equilibrium contact angles.

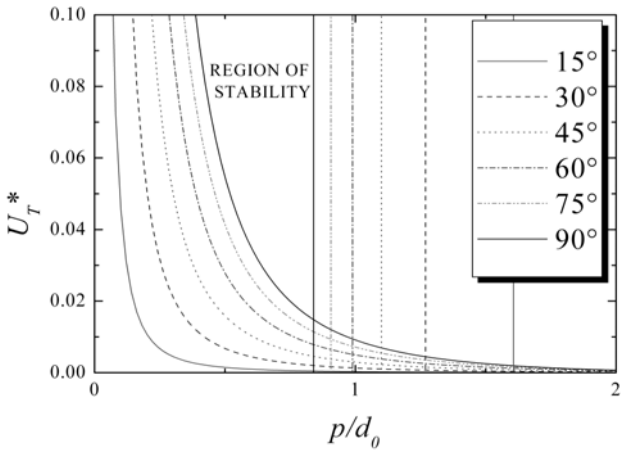

Figure 11. Alternative representation of the regions within which inkjet printed liquid lines or beads are stable using dimensionless axes of velocity and drop spacing for a range of contact angles. The curved lines show the onset of the bulging instability and the vertical lines show the limit of maximum droplet spacing. The region of stability clearly gets smaller and the range of stable droplet spacing reduces as the contact angle increases.

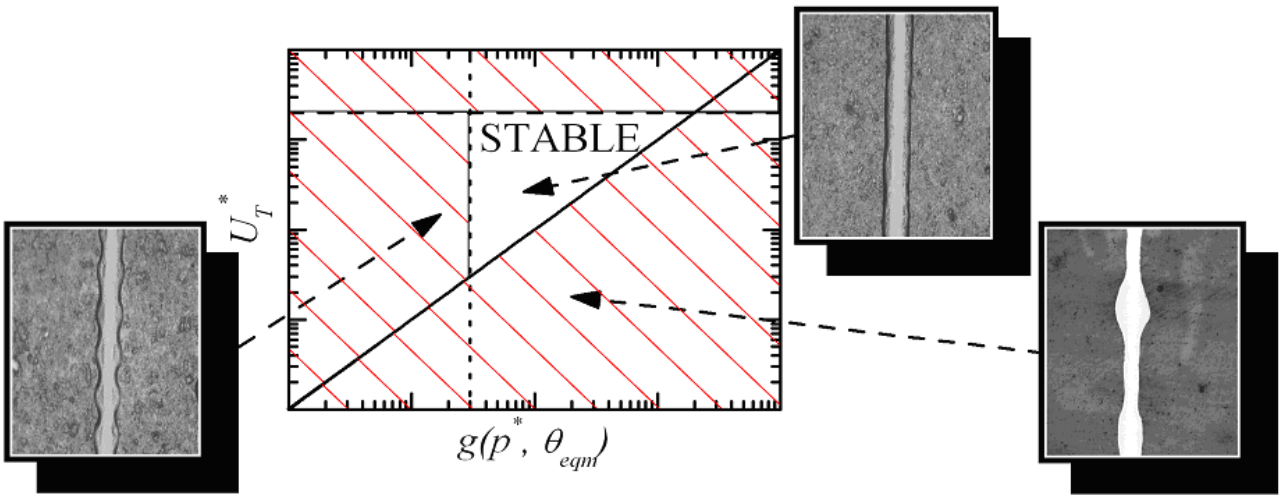

TOC Image